"Electrochemical Shock" of Intercalation Electrodes: A Fracture Mechanics Analysis

"Electrochemical Shock" of Intercalation Electrodes: A Fracture Mechanics Analysis

William H. Woodford, Yet-Ming Chiang,* and W. Craig Carter[z]

Department of Materials Science and Engineering, Massachusetts Institute of Technology, Cambridge, Massachusetts 02139, USA

Fracture of electrode particles due to diffusion-induced stress has been implicated as a possible mechanism for capacity fade and impedance growth in lithium-ion batteries. In brittle materials, including many lithium intercalation materials, knowledge of the stress profile is necessary but insufficient to predict fracture events. We derive a fracture mechanics failure criterion for individual electrode particles and demonstrate its utility with a model system, galvanostatic charging of $Li_xMn_2O_4$. Fracture mechanics predicts a critical C-rate above which active particles fracture; this critical C-rate decreases with increasing particle size. We produce an electrochemical shock map, a graphical tool that shows regimes of failure depending on C-rate, particle size, and the material's inherent fracture toughness K_{Ic}. Fracture dynamics are sensitive to the gradient of diffusion-induced stresses at the crack tip; as a consequence, small initial flaws grow unstably and are therefore potentially more damaging than larger initial flaws, which grow stably.

Rechargeable batteries, especially lithium-ion batteries, are beginning to enable new paradigms in transportation and renewable energy. Essential to the success of these endeavors are assurances of performance and reliability, which in turn require that the underlying degradation phenomena that limit battery life be properly understood. Mechanical fracture has been implicated as a possible mechanism for capacity fade and impedance growth in lithium-ion batteries.[1] Particle level fracture has been observed in postmortem electron microscopy studies of intercalation materials[2-5] and is claimed as a source of acoustic emission during cycling.[6,7] Models with realistic fracture criteria are needed to understand the role of fracture in electrode degradation and to design mechanically robust electrodes and, potentially, life-prolonging duty cycles. This is especially critical for high storage capacity materials such as silicon, tin, and their alloys,[8] and displacement reaction storage materials such as oxides[9,10] and fluorides.[11]

Some prior models of mechanical degradation have calculated diffusion-induced stresses, which arise from dimensional changes due to variations in composition, for battery electrode materials subjected to common electrochemical protocols. García et al. developed a two-dimensional (2D) finite element model to calculate stress profiles in composite electrodes.[12] Cheng and Verbrugge derived analytical expressions for stress evolution in spherical particles under potentiostatic and galvanostatic operation and have included surface effects in their calculation of stresses in nanoscale electrode particles.[13,14] Golmon et al. used a homogenization approach to model composite electrodes and explored the effects of externally applied loads and electrode porosity.[15] Renganathan et al. used a quasi-2D porous electrode model for $LiCoO_2$/graphite cells to evaluate stresses caused by compositional inhomogeneities and phase transformations.[16]

Other models have suggested certain failure criteria to predict particle fracture caused by diffusion-induced stresses, but fracture mechanics criteria were not proposed or implemented. Christensen and Newman derived a detailed general model for diffusion-induced stresses in intercalation electrodes that includes elastodiffusion coupling, nonideal solution thermodynamics, and nonlinear partial molar volume.[17,18] They suggested a "tensile yield stress" criterion (assumed to be the same everywhere within the electrode) to predict the onset of fracture. Christensen has since incorporated the diffusion-induced stress model, again using a tensile yield stress failure criterion, in a quasi-2D porous electrode (Dualfoil) model of $LiMn_2O_4$/mesocarbon microbead cells.[19] Zhang et al. implemented a numerical elastodiffusion model to calculate diffusion-induced

stresses in spherical and ellipsoidal electrode particles[20,21] but suggested the von Mises equivalent stress as a predictor of electrode failure. Cheng and Verbrugge have also proposed a single value of maximum tensile stress to predict fracture[22] due to diffusion-induced stress.

In typical lithium intercalation compounds, knowledge of the diffusion-induced stress profile is necessary but insufficient to predict fracture. Yield stress and von Mises equivalent stress failure criteria are not well defined for brittle materials. These concepts from continuum plasticity theory are most appropriate for materials that undergo dislocation-mediated plastic deformation; they are yield, not fracture criteria. Instead, linear elastic fracture mechanics can provide a unique failure criterion in terms of the stress intensity factor, which incorporates both the stress profile and the pre-existing flaw population.

There is a separate body of literature where fracture mechanics analysis has been applied to the mechanical degradation of lithium alloy electrodes. In contrast to the above-cited work, diffusion-induced stresses, due to composition gradients, have not been included as the driving force for fracture. Huggins and Nix developed a one-dimensional model for fracture of thin-film alloy electrodes undergoing a first-order phase transformation.[23] Wolfenstine proposed a critical grain size model for microcracking due to lithiation of tin[24] and with collaborators, measured the fracture toughness of Li_xSn alloys.[25] Aifantis et al. modeled radial cracking in composite anodes composed of active particles embedded in inert matrices.[26-28] Most recently, Hu et al. modeled cracks in two-phase $LiFePO_4$/$FePO_4$ particles with interface coherency stresses with fully anisotropic elastic constants and stress-free strains.[29]

The objective of the present study is to derive a fracture mechanics failure criterion for electrochemical systems having diffusion-induced stresses due to composition gradients. Here, we both calculate diffusion-induced stresses and use linear elastic fracture mechanics to predict fracture events. This approach gives a physically appropriate failure criterion for a large class of brittle electrode materials subjected to typical electrochemical duty cycles. Recently, Bhandakkar and Gao developed a cohesive model for crack nucleation in thin strip electrodes subjected to galvanostatic cycling; they find a critical size below which cracks do not nucleate.[30] We instead study the growth of a pre-existing dominant flaw in a single-particle electrode.

We propose the name "electrochemical shock" for fracture driven by diffusion-induced stresses in electrode materials because of the close analogy to thermal shock of brittle materials. Thermal shock refers to fracture due to thermoelastic stresses caused by rapid heating or cooling. Hasselman framed thermal shock in terms of fracture mechanics.[31] A more detailed and recent analysis is given by Bahr et al.[32-35]

---

* Electrochemical Society Active Member.
[z] E-mail: ccarter@mit.edu

$$J = -D\left(\nabla c - \frac{\Omega c}{RT}\nabla\sigma_h\right) = -D(1 + \theta c)\nabla c \qquad [2]$$

The second equality in Eq. 2 allows the stress-coupling effect to be recast as a concentration-dependent diffusivity. The parameter θ measures the stress-coupling effect and is given by

$$\theta = \frac{2\Omega^2 E}{9RT(1 - \nu)} \qquad [3]$$

For galvanostatic charging, the boundary conditions are zero flux at the particle center and constant flux proportional to the surface current density i_n normal to the particle surface

$$\left.\frac{\partial c}{\partial r}\right|_{r=0} = 0 \qquad \left.\frac{\partial c}{\partial r}\right|_{r=r_{max}} = \frac{-i_n}{D\mathcal{F}(1 + \theta c)} \qquad [4]$$

and the initial condition is the uniform concentration in the fully lithiated (discharged) state

$$c(r, t = 0) = c_{max} \qquad [5]$$

To perform numerical calculations and report their results, we use the dimensionless variables suggested by Zhang et al.

$$\hat{c} = \frac{c}{c_{max}} \qquad \hat{r} = \frac{r}{r_{max}} \qquad \hat{t} = \frac{tD}{r_{max}^2} \qquad [6]$$

$$\hat{\theta} = \theta c_{max} = \frac{2\Omega^2 E c_{max}}{9RT(1 - \nu)} \qquad [7]$$

$$\hat{I} = \frac{i_n r_{max}}{Dc_{max}\mathcal{F}} = \frac{(C\ \text{rate})\alpha\rho r_{max}^2}{3Dc_{max}\mathcal{F}} \qquad [8]$$

The second equality in Eq. 8 comes from the relationship between the surface current density and C-rate for an individual spherical particle

$$i_n = (C\ \text{rate})\left(\frac{\alpha\rho r_{max}}{3}\right) \qquad [9]$$

C-rate describes the normalized charging rate of a cell and has units of h^{-1}. A C/n charge accumulates the full theoretical capacity of a cell in n hours. For example, a cell charged at a 2C-rate reaches its theoretical capacity in 30 min.

The boundary value problem is solved numerically using the built-in pdepe solver in MATLAB. The spherical particle is discretized into 10,000 spatial points and the time stepping is handled automatically by the built-in ode15s adaptive time integrator. Each simulation was run until the dimensionless concentration at the particle surface, $\hat{c}(\hat{r} = 1, \hat{t}_{final})$ was less than 10^{-6}.

The diffusion-induced stresses are calculated by solving a linear elastic boundary value problem analogous to the calculation of thermal stresses. We relate the composition and stress profiles following Timoshenko and Goodier's method of calculating thermal stresses.[36] The resulting stress-composition relationships match those used by Cheng and Verbrugge.[14]

First, we define the average concentration within a sphere of radius r, where $r \leq r_{max}$, as

$$c_{av}(r, t) = \frac{3}{r^3}\int_0^r c(r, t)r^2 dr \qquad [10]$$

Assuming isotropic linear elasticity and traction-free boundaries, the radial and tangential stress profiles are given by

$$\sigma_r(r, t) = \frac{2\Omega E}{9(1 - \nu)}[c_{av}(r_{max}, t) - c_{av}(r, t)] \qquad [11]$$

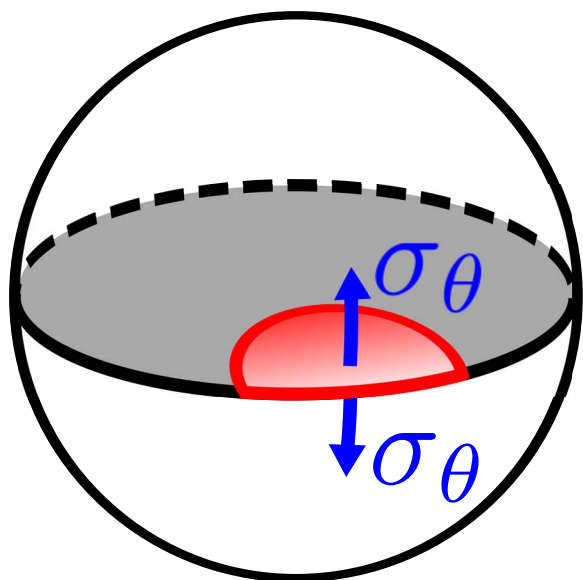**Figure 1.** (Color online) Geometry of a semicircular crack on the surface of a spherical electrode particle. A tensile tangential stress σ_θ acts to increase the size of the crack.

Methods

To develop and quantify a fracture mechanics failure criterion for electrochemical shock, we use individual spherical particles of $Li_xMn_2O_4$ as a model system. We postulate that each particle of radius r_{max} contains a finite-sized semielliptical surface crack of length a, as shown in Fig. 1. To facilitate this model, we make a few simplifying assumptions. First, we assume that the crack faces are electrochemically inert so that only the spherical outer surface of the particle is reactive. Second, we treat $Li_xMn_2O_4$ as a continuous solid solution $0 \leq x \leq 1$ with elastic and fracture properties that are constant across the full composition range.

We use a two-step method to determine the stress intensity factor $K_I(a, t)$, defined in the stress intensity factor section, caused by galvanostatic charging. First, we calculate diffusion-induced stress profiles over a range of galvanostatic charge rates using a numerical elastodiffusion model. Then, we use the diffusion-induced stress profiles at the end of charging to calculate the stress intensity factor as a function of flaw size. It is possible that particles fracture at an intermediate time during charge, but the end-of-charge stress intensity factor is useful to predict fracture through the entire charging cycle. The calculated stress intensity factors are used to predict fracture for a wide range of C-rate and particle size combinations. The stress intensity factor–flaw size relationships are examined in detail to assess the dynamics of crack growth.

Elastodiffusion model.— To calculate diffusion-induced stress profiles, we implement a modified version of the numerical elasto-diffusion model of Zhang et al.[21] All symbols presented in the text are also defined in the List of Symbols at the end of the paper. We repeat only the essential features of the original model that are necessary to understand the present work. We solve the diffusion equation

$$\frac{\partial c}{\partial t} = -\nabla\cdot J \qquad [1]$$

with a flux driven by gradients in concentration and hydrostatic stress

Table I. Material properties of LiMn$_2$O$_4$ used in calculations.

Property	Symbol	Units	Value
Young's modulus	E	GPa	200
Poisson's ratio	ν	—	0.3
Lithium diffusivity	D	cm^2/s	2.2×10^{-9}
Partial molar volume of lithium	Ω	cm^3/mol	3.26
Maximum lithium concentration	c_{max}	mol/m^3	2.37×10^4
Density	ρ	g/cm^3	4.28
Theoretical capacity	α	mAh/g	148
Temperature	T	K	300

$$\sigma_\theta(r,t) = \frac{\Omega E}{9(1-\nu)}[2c_{av}(r_{max},t) + c_{av}(r,t) - 3c(r,t)] \quad [12]$$

Numerical calculations are done in terms of the dimensionless stresses

$$\hat{\sigma}_r = \frac{\sigma_r}{E} \quad \hat{\sigma}_\theta = \frac{\sigma_\theta}{E} \quad [13]$$

Our Eq. 11 and 12 differ from the corresponding expressions of Zhang et al. because we take any state of uniform composition to be stress-free, matching the assumption of traction-free boundaries. That is, diffusion-induced stresses in our model arise only from internal composition gradients, not from overall changes in composition. These results are directly applicable to single-phase materials, where stresses arise from composition gradients. Future modifications will include first-order phase transformations or interface coherency stresses.

Materials properties.— The Young's modulus and lithium diffusivity that we supply as inputs to the elastodiffusion model also differ significantly from those used by Zhang et al. First, it is believed that the value of the Young's modulus (10 GPa) that Zhang et al.[21] and Christensen and Newman[18] used to calculate diffusion-induced stress in LiMn$_2$O$_4$ is roughly 1 order of magnitude too low given the structure and composition of this material. The original source of this value is Paolone et al. who reported the results of anelastic spectroscopy on porous sintered polycrystalline samples.[37]

Instead, we have used a Young's modulus of $E = 200$ GPa in our calculations. Grechnev et al. calculated a bulk modulus of $B \approx 200$ GPa for LiMn$_2$O$_4$ using ab initio methods.[38] For elastically isotropic materials, the bulk and Young's moduli are related by

$$E = 3B(1 - 2\nu) \quad [14]$$

Taking a Poisson's ratio of $\nu = 0.3$, the corresponding Young's modulus is 240 GPa, much higher than the value reported by Paolone et al. As many other spinel oxides have $E \approx 100–300$ GPa,[39,40] $E = 200$ GPa seems a reasonable estimate of the true value for LiMn$_2$O$_4$.

We take the lithium diffusivity to be 2.2×10^{-9} cm^2/s, the reported best fit value from a single-particle electrochemical model of LiMn$_2$O$_4$.[41] The complete set of material properties used as model inputs is given in Table I. The material properties used in the present study give a dimensionless stress-coupling parameter $\hat{\theta} = 6.397$, almost 20 times larger than the corresponding value of Zhang et al., $\hat{\theta}_{Zhang} = 0.3564$.

Stress intensity factor.— Linear elastic fracture mechanics provides a deterministic failure criterion in terms of the stress intensity factor, which characterizes stress concentration ahead of a flaw. For the simple case of uniform tension, a material subjected to a stress σ containing a single flaw of characteristic size a experiences a stress intensity factor $K = Y\sigma\sqrt{\pi a}$, where Y is a dimensionless geometric factor. The stress intensity factor is conventionally expressed in SI units of MPa m$^{1/2}$. For a classical reference on fracture mechanics, see the text by Lawn.[42]
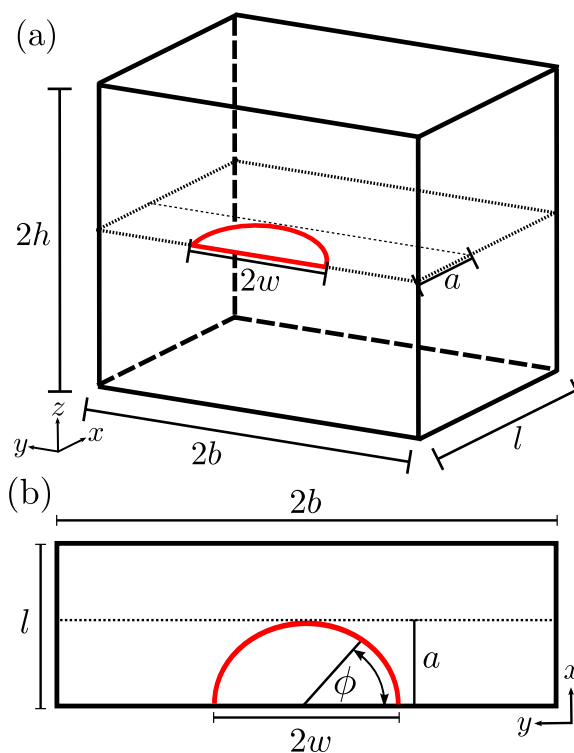

Figure 2. (Color online) Geometry of plate model used to calculate stress intensity factors under the nonuniform stress profiles calculated from elasto-diffusion model. (a) Full view of plate. (b) Plan view of the crack plane. To match the plate and sphere models, we take $l = r_{max}$, $b = \pi r_{max}$, and $h = \pi r_{max}$. As a simplifying case, we consider only semicircular cracks where $w = a$.

A material's resistance to crack growth is described by a critical value of the stress intensity factor (K_{Ic}) known as the fracture toughness. When the applied stress intensity factor exceeds the material's fracture toughness, the pre-existing crack grows. The fracture toughness is a material property, whereas the fracture strength, that is, the stress necessary to induce crack growth, is not. Fracture strength depends on flaw geometry, loading conditions, and material properties. The crack propagation criterion in linear elastic fracture mechanics is consistent with thermodynamic free energy minimization. This criterion embodies the competition between a driving force from elastic strain energy, enhanced by the stress concentration around flaws, and a resistance due to the creation of fresh surface area. Models that assume a single threshold stress as a fracture criterion do not reflect the minimum free energy configuration for the system and therefore do not accurately predict fracture.

In brittle materials, surface flaws subjected to tensile stresses are the most common origin of catastrophic failure. For this reason, we simulate charging (deintercalation) of Li$_x$Mn$_2$O$_4$, which produces tensile tangential stresses (because the partial molar volume of lithium in this material is positive) that tend to open the surface flaws, as illustrated in Fig. 1. The fracture toughness of Li$_x$Mn$_2$O$_4$ is presently unknown, but can be determined experimentally. When this value is needed for analysis, we present results for a range of fracture toughness values representative of brittle materials.

We calculate stress intensity factors using the method of weight functions and an edge-cracked plate approximating geometry shown in Fig. 2. The dimensions of the plate are related to those of the sphere as

$$l = r_{max} \quad b = \pi r_{max} \quad h = \pi r_{max} \quad [15]$$

The stress intensity factor of this plate under uniform tensile loading is used as the reference case for the method of weight functions,

details of which are provided in the Appendix. This geometric approximation avoids an unrealistic assumption of a uniform stress profile yet does not require the intricacy of a full-scale finite element model. This approximation does not affect the character of the solution (i.e., the scaling with respect to flaw size and material parameters) and therefore serves to provide qualitative insight on the behavior of cracks subjected to nonuniform diffusion-induced stress profiles.

The stress intensity factor for this electrochemical shock problem can be calculated following the approach of Mattheck[43] by the integral equation

$$K_I = \frac{E}{K_{ref}(1 - \nu^2)} \int_0^a \sigma_\theta(x) m(x,a) dx \qquad [16]$$

where K_{ref} is the reference stress intensity factor and $m(x,a)$ is the weight function (a kernel or Green's function) against which the diffusion-induced stress profile is integrated.

An essential feature of Eq. 16 is that the stress distribution is integrated over the entire crack length; this means that the spatial variation in the stress profile matters. A moderate, uniform stress profile can induce a stress intensity factor greater than a sharply peaked but rapidly decreasing stress profile; this effect is important for electrochemical shock at large currents. To generate a large stress intensity factor, the diffusion-induced stress must be large at the crack tip, not just at the particle surface. The weight function $m(x,a)$ is characteristic of the reference case; more details are given in the Appendix and the original literature.[43,44]

The stress distribution $\sigma_\theta(x)$ is the tangential component of the diffusion-induced stress at the end of charge ($t = t_f$) subject to the change in variables $x = r_{max} - r$. The reference case is uniform tensile loading in the *z*-direction of the semielliptical surface cracked plate.[45] The stress intensity factor calculated in this way is a function of crack dimensions a and w and the angle ϕ, all shown in Fig. 2b. As a simplifying case, we restrict our analysis to semicircular cracks with $w = a$. Results not presented here show that $\phi = 0$ (and $\phi = \pi$, as required by the symmetry of the problem) is the direction of maximum stress intensity factor, so we consider only this direction. We neglect mode II and III crack face loading because the material's other toughness values, K_{IIc} and K_{IIIc}, are generally much larger than K_{Ic}. For numerical calculations, we make the problem dimensionless by normalizing all lengths to the particle radius and we introduce the dimensionless stress intensity factor

$$\hat{K}_I = \frac{K_I}{E\sqrt{r_{max}}} \qquad [17]$$

Results and Discussion

To provide a concrete picture of our results, we take as an illustrative example the simulation with $\hat{I} = 0.92$, embodied as a 5C galvanostatic charge of a 21 μm particle and provide dimensionalized (i.e., physical units of measure) results. The results highlighted by this example hold generally for galvanostatic electrochemical shock. Figure 3 shows the time evolution of the tangential stress profile at five different radial positions during the 5C charge. As expected for deintercalation of a material with a positive partial molar volume of lithium, the surface tangential stress is tensile (positive), whereas the tangential stress at the particle center is compressive. The spatial profile would be reversed for discharge or if the partial molar volume was negative. The tangential stress shows rapid changes at the beginning and end of cycling, which is reflective of the assumption of ideal solution behavior underlying Eq. 2. The spread between maximum and minimum tangential stresses increases monotonically throughout the charging process.

The tangential stress profile at the end of charge is the key link between the elastodiffusion model and the stress intensity factor model. We take the end-of-charge state as the surface lithium concentration going to zero, which physically corresponds to a voltage
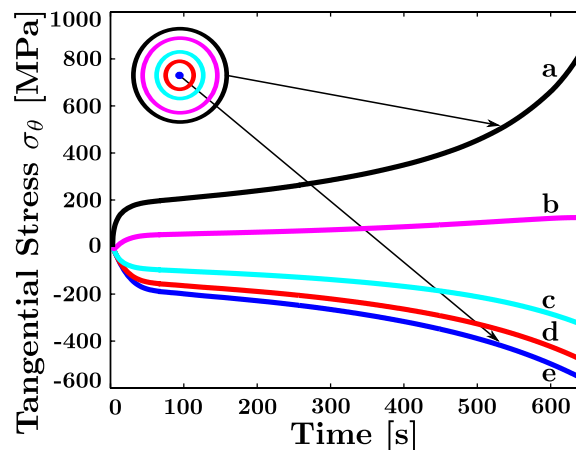

Figure 3. (Color online) Evolving tangential stress profile for the condition $\hat{I} = 0.92$ embodied as a 5C charge of a 21 μm particle. Each curve represents a different radial position in the particle: (a) $\hat{r} = 1$ (particle surface), (b) $\hat{r} = 0.8$, (c) $\hat{r} = 0.5$, (d) $\hat{r} = 0.3$, and (e) $\hat{r} = 0$ (particle center).

cutoff for constant-current charging. After reaching this state, charging may be terminated, allowing the particle to relax to a state of uniform lithium concentration, or charging may continue under a potential-controlled step, a so-called constant-current constant-voltage charge sequence. We do not study the additional potential-controlled step, but it is a natural extension of this work.

It is likely that particles fracture at an intermediate time during galvanostatic charging; the end-of-charge state gives the most severe loading condition and is therefore used to predict if fracture is possible for a given set of conditions. If a particular instantaneous stress profile and crack length would cause fracture at the intermediate time, our model still predicts fracture for that particle at the end-of-charge state. We do not attempt to predict the temporal rate of fracture events; we seek only to predict if fracture is an energetically favorable event.

Figure 4 shows the tangential stress (curve a, blue, left axis) and composition (curve b, red, right axis) profiles at the end of charging for the same $\hat{I} = 0.92$ example case. The gradients of both the composition and tangential stress profiles are most severe near the particle surface ($r = 21$ μm) and least severe near the center of the particle ($r = 0$). The area under the composition curve indicates that there is substantial unused capacity at the end of the galvanostatic
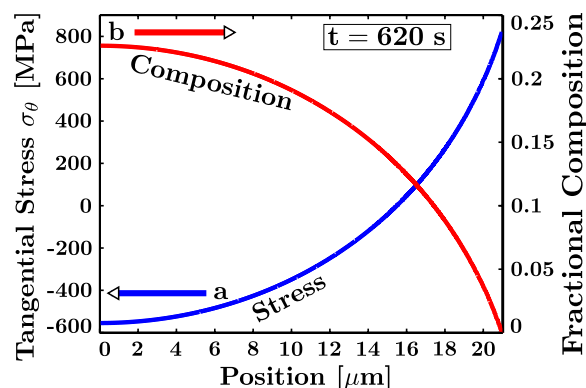

Figure 4. (Color online) (a) Tangential stress profile and (b) composition profile at the end of charge for the condition $\hat{I} = 0.92$ embodied as a 5C charge of a 21 μm particle. This tangential stress profile is used to calculate the stress intensity factors shown in Fig. 5.
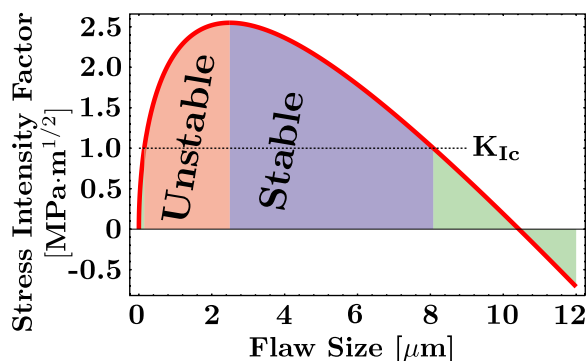
Figure 5. (Color online) Stress intensity factor K_I increases rapidly for small flaws but quickly reaches a maximum and decreases, becoming negative for very large flaws. The dashed horizontal lines represent a plausible value of fracture toughness, $K_{Ic} = 1$ MPa m$^{1/2}$; the shading represents regions of unstable and stable crack growth dynamics, explained in the text. This calculation represents $\hat{I} = 0.92$ embodied as a 5C charge of a 21 μm particle.

charge. A subsequent constant voltage charging step would extract some of this remaining lithium from the electrode.

Each calculated stress intensity factor–flaw size relationship has a maximum that places a lower bound on the combinations of particle size and C-rate that can cause fracture. To explain the meaning of this lower bound, consider the stress intensity factor–flaw size relationship for the $\hat{I} = 0.92$ example case shown in Fig. 5. For this example case, fracture is never expected, for any pre-existing flaw size, if the fracture toughness is greater than ~ 2.5 MPa m$^{1/2}$. If the fracture toughness is 1 MPa m$^{1/2}$, shown by the dashed horizontal lines in Fig. 5, pre-existing flaws between ~ 0.25 and ~ 8 μm grow. The shading under the curve, explained later, delineates the crack growth dynamical modes for $K_{Ic} = 1$ MPa m$^{1/2}$. Again, the fracture toughness of Li$_x$Mn$_2$O$_4$ is presently unknown but can be determined experimentally. Generalizing from this particular example, fracture only occurs if the maximum stress intensity factor for a given particle size and C-rate exceeds the material's inherent fracture toughness. Fracture does not occur if the maximum stress intensity factor for a particular particle size and C-rate does not exceed the fracture toughness.

The example case shown in Fig. 3-5 demonstrates why a fracture mechanics criterion is required to predict electrochemical shock. As shown in Fig. 3, the maximum tangential stress in this particle is nearly 800 MPa, greatly exceeding any proposed tensile fracture stress. However, as argued in the preceding paragraph, this particle does not fracture if the fracture toughness of LiMn$_2$O$_4$ is greater than 2.5 MPa m$^{1/2}$. This shows that the spatial variation in the stress profile throughout the particle, not just the peak tensile stress, determines the likelihood of fracture. Again generalizing from this example, the fracture mechanics criterion predicts that intercalation electrodes are likely more resilient to electrochemical shock than tensile stress criteria suggest.

We apply the fracture mechanics criterion for electrochemical shock across a wide range of particle sizes and C-rates using the dimensionless current and dimensionless stress intensity factor. Figure 6 shows that the maximum dimensionless stress intensity factor initially increases with dimensionless current across several orders of magnitude but decreases at very high dimensionless currents. The increase is easily understood as an overall increase in the diffusion-induced tangential stress as the current increases. The decrease can be explained as a "skin" effect: Although the nominal maximum stresses may be large, the tensile stress field rapidly decays through a thin region near the particle surface. Therefore, only the smallest flaws, those with their crack tip in the vicinity of the surface, are affected and the maximum stress intensity factor is diminished.

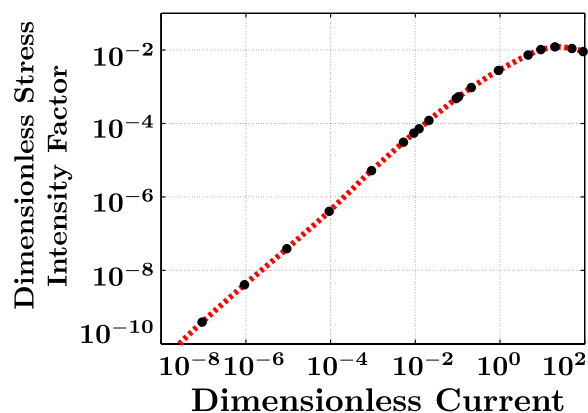Figure 7 shows the critical combinations of particle size and

Figure 6. (Color online) The maximum dimensionless stress intensity factor $\hat{K}_I$ increases with dimensionless current $\hat{I}$ for small to moderate values of $\hat{I}$ but decreases somewhat at very large values of $\hat{I}$. The turnover is attributed to a skin effect, where only shallow surface flaws are subjected to tensile diffusion-induced stresses. The black points represent computation results and the dashed red curve indicates a cubic spline interpolating function.

C-rate that can cause fracture during galvanostatic charging. This figure, which we call an electrochemical shock map, gives a simple picture of fracture-safe and fracture-likely conditions. As proxies for the unknown fracture toughness of LiMn$_2$O$_4$, we plot five values of fracture toughness representative of brittle materials: (a) 0.1, (b) 1, (c) 3, (d) 5, and (e) 10 MPa m$^{1/2}$. For comparison, the fracture toughness of soda-lime-silicate glass is ~ 1 MPa m$^{1/2}$, the single-crystal fracture toughness of magnesium aluminate spinel (MgAl$_2$O$_4$) is 1.2–1.9 MPa m$^{1/2}$,[46] and the fracture toughness of single-crystal sapphire (α-Al$_2$O$_3$) is 2.4–4.5 MPa m$^{1/2}$.[47] The range of values for MgAl$_2$O$_4$ and α-Al$_2$O$_3$ is due to the crystallographic anisotropy of the single-crystal fracture toughness in these materials. We anticipate that the fracture toughness of LiMn$_2$O$_4$ is within this range of values. Combinations of particle size and C-rate lying below (and to the left of) the curve for the fracture toughness
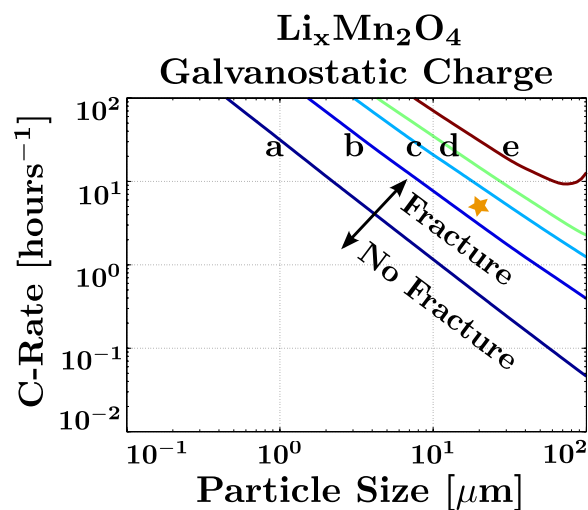
Figure 7. (Color online) Electrochemical shock map for galvanostatic charging of Li$_x$Mn$_2$O$_4$ on logarithmic axes. Curves represent the onset of fracture for five representative values of the fracture toughness (K_{Ic}) of brittle materials: (a) 0.1, (b) 1, (c) 3, (d) 5, and (e) 10 MPa m$^{1/2}$. Above the curve representing each value of fracture toughness, fracture is possible. The orange star represents the example case shown in Fig. 3-5.

of LiMn$_2$O$_4$ do not induce fracture; conditions lying above (and to the right of) the curve may cause fracture, depending on the pre-existing flaw size.

The example case shown in Fig. 3-5 is indicated on the electro-chemical shock map (Fig. 7) as an orange star. The position of the star shows that this particle is subject to fracture if the fracture toughness is (a) 0.1 or (b) 1 MPa m$^{1/2}$ but does not fracture if the fracture toughness is (c) 3, (d) 5, or (e) 10 MPa m$^{1/2}$.

The general trend of decreasing critical C-rate with increasing particle size matches our intuition that large particles subjected to fast charges are most readily damaged. Furthermore, the skin effect is manifested in the upward bowing of curve (e) for K_{Ic} = 10 MPa m$^{1/2}$ in Fig. 7. The skin effect appears first along the particle size axis because the dimensionless current scales quadrati-cally with particle size but linearly with C-rate. The fracture me-chanics analysis suggests that electrochemical shock can be pre-vented by limiting particle size or by optimizing electrochemical charging routines.

Using a controlled variable current charge, starting from a low rate and building to a high rate, it may be possible to charge rapidly without inducing fracture. The low initial rate builds a reservoir of composition in the center of the particle that limits the maximum concentration gradient inside the particle as the charge is ramped to higher rates.

The accuracy of electrochemical shock prediction is currently limited by uncertainty in lithium diffusivity data. Reported values for our model compound LiMn$_2$O$_4$ span at least 3 orders of magni-tude, as summarized in Table III of Ref. 41. Although the diffusivity used in the present study was the best fit value from Zhang's analysis,[41] it is larger than some other reported values. A lower diffusivity value would lead to fracture at lower rates and/or smaller particle sizes than those predicted in Fig. 7, whereas a greater dif-fusivity would have the opposite effect. To accurately predict elec-trochemical shock, we seek better experimental diffusivity data.

This fracture mechanics model could also be integrated into a porous electrode model to predict mechanical damage accumulation in composite battery electrodes. The C-rate in Fig. 7 refers to the local single-particle C-rate, not the homogenized macroscopic C-rate describing a composite electrode. In a composite electrode, there may be spatial inhomogeneities in the current density, espe-cially in the thickness direction. If we have a model for the current distribution of a porous composite electrode, this fracture model can be applied to predict fracture of individual active particles compos-ing that electrode. Integration of this model with a conventional porous electrode theory would mirror the approach of Christensen[19] and Renganathan et al.[16]

Returning to Fig. 5, we find that crack growth due to diffusion-induced stress can be stable or unstable, depending on the initial flaw size. Fracture mechanics predicts unstable crack growth when

$$K_I > K_{Ic} \qquad [18]$$

and

$$\frac{\partial K_I}{\partial a} > \frac{\partial K_{Ic}}{\partial a} \qquad [19]$$

Physically, these conditions imply that crack growth is unstable when the stress intensity factor exceeds the fracture toughness and the crack growth driving force increases as the crack grows. Cracks that grow unstably accumulate kinetic energy that causes them to grow beyond any secondary stable length; this is one mechanism by which terminal failure may occur.

Counterintuitively, small initial flaws, those flaws smaller than the crack length corresponding to the maximum stress intensity fac-tor, may be more damaging than larger initial flaws because small flaws grow unstably. Our intuition fails because small cracks feel only the large tangential stresses near the particle surface. As the tangential stress decreases rapidly through the particle, the crack tips of larger flaws experience less severe opening loads. Again, this demonstrates that the spatial variation in the stress profile is impor-
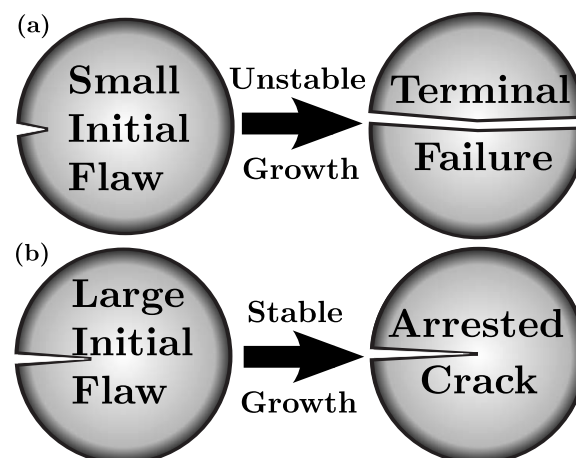

Figure 8. (a) Small initial flaws (those to the left of the maximum in Fig. 5) grow unstably and can cause terminal failure of electrode particles, whereas (b) large initial flaws (those to the right of the maximum in Fig. 5) grow stably and the crack arrests at a final length ($a_{arrested}$), where $K_I(a_{arrested}, t_{final}) = K_{Ic}$.

tant to electrochemical shock prediction. The initial rapid increase in stress intensity factor in Fig. 5 satisfies the conditions for unstable crack growth, assuming that the fracture toughness does not increase rapidly with flaw size. As these cracks begin to grow, they experi-ence an even greater crack growth driving force. This gives the cracks kinetic energy, which causes them to grow beyond any sec-ond length where $K_I = K_{Ic}$. The excess kinetic energy can be suffi-cient to cause the crack to grow through the particle to another free boundary, causing terminal failure. One can envision that terminal particle failure due to unstable crack growth may cause isolation of active material from the conductive network in a composite elec-trode, thereby contributing to electrode degradation.

In contrast, large flaws, those flaws larger than the sizes corre-sponding to the maximum stress intensity factor, grow stably to a length that satisfies $K_I = K_{Ic}$, where crack growth is arrested. Al-though terminal failure is unlikely for flaws that grow stably, the increased surface area may still have a deleterious effect on elec-trode performance and lifetime.

This difference in crack growth dynamics depends only on the pre-existing flaw size. Consider two identically sized particles sub-jected to galvanostatic charging at the same C-rate, one with a very large flaw and the other with a small flaw. The particle with the larger flaw undergoes stable crack growth to some final length, where the crack arrests. The particle with the smaller flaw undergoes unstable crack growth, which may cause terminal failure of the par-ticle. Figure 8 compares schematically the anticipated consequences of (a) unstable and (b) stable crack growth dynamics associated with small and large initial flaws, respectively. This picture of stable and unstable crack growth matches Hasselman's classic result for ther-mal shock, where small initial flaws have a more deleterious effect on the strength of brittle materials subject to rapid thermal quenching.[31] Our fracture mechanics model preserves the analogy between thermal and diffusion-induced stresses, which was used to solve the elastic boundary value problem.

The shading in Fig. 5 corresponds to the crack growth dynamics for K_{Ic} = 1 MPa m$^{1/2}$: green for no crack growth, red for unstable crack growth, and blue for stable crack growth. The two crack growth dynamical modes are separated by the maximum in the stress intensity factor–flaw size relationship.

Although we have not incorporated the statistical nature of flaw size distributions, it significantly impacts the mechanical durability of real electrode materials. Our model assumes the existence of a single largest pre-existing flaw in a given particle. Flaw populations in most materials are well described by Weibull statistics, where the

probability of finding a "large" flaw scales rapidly with the volume of material. A Weibull model for the flaw distribution could be used when extending this model to real composite electrodes containing many individual active particles.

Fatigue may promote mechanical failure if subcritical cracks (i.e., those having stress intensity factor less than the fracture toughness) are present. Cyclic charging and discharging cycles induce cyclic tension and compression, which is known to promote subcritical crack growth. The rate of subcritical crack growth is characterized by the empirical relationship known as Paris' Law, expressed as

$$\frac{da}{dN} = C_{\mathrm{Paris}} \cdot \Delta K^p \qquad [20]$$

where C_{Paris} and p are empirical parameters. Repeated cycling causes the initially small crack to grow until its stress intensity factor reaches the fracture toughness and unstable crack growth and, potentially, terminal failure as was discussed previously, occurs. The method developed in this study can be used to calculate ΔK for different charge–discharge cycles to predict fracture events throughout the life of an intercalation electrode. Experience in fatigue crack growth in brittle materials shows that C_{Paris} and p are sensitive to small changes in environmental conditions. Because the crack tip is an electrochemically active environment, such sensitivity should be expected in electrochemical shock.

In summary, we have derived a fracture model to predict electrochemical shock using particle size and C-rate as inputs. We used a numerical elastodiffusion model to predict coupled composition and stress profiles for individual spherical particles. Then, we use our fracture mechanics model to calculate the corresponding stress intensity factor–flaw size relationships. The fracture mechanics model is general enough to be integrated with any model for diffusion-induced stress, including those of Garcìa et al.,[12] Christensen and Newman,[17,18] or Cheng and Verbrugge.[13,14] This integration would provide a fracture mechanics failure criterion for those stress models and could be used to extend the applicability of our model to include nonideal solution thermodynamics, nonlinear partial molar volume, and phase transformations.

Conclusions

Fracture mechanics predicts a critical C-rate for fracture during galvanostatic charging, which decreases with increasing particle size. We show the critical combinations of C-rate and particle size for the model system Li$_x$Mn$_2$O$_4$ on an electrochemical shock map, which shows the division between fracture-safe and fracture-likely conditions. Electrochemical shock maps can be used as a material selection tool; as one simple example, a designer given a required C-rate could identify mechanically durable electrode active materials and particle sizes on the map.

The fracture mechanics analysis shows that electrode particles are likely more resilient to electrochemical shock than tensile stress criteria have suggested. The highly nonuniform tangential stress profiles caused by galvanostatic charging produce a maximum stress intensity factor for a given combination of C-rate and particle size. In cases where the maximum stress intensity factor is less than the fracture toughness of the material, fracture does not occur; however, fatigue may cause subcritical flaws to grow and produce larger stress intensities. In cases where the maximum stress intensity factor exceeds the fracture toughness of the material, pre-existing cracks grow; small pre-existing cracks grow unstably and larger pre-existing flaws grow stably. Due to the difference in growth dynamics, we can envision scenarios where small flaws have a more deleterious effect on battery lifetime than large flaws.

The dependence of stress intensity factor on both particle size and galvanostatic charge rate suggests that electrochemical shock can be avoided by tailoring the microstructure and charging profiles of intercalation electrodes to minimize the diffusion-induced stress intensity factor.

List of Symbols

a	crack length
b	plate half-width
B	bulk modulus
c	lithium concentration
c_{av}	average concentration in a sphere
c_{max}	maximum lithium concentration
$\hat{c}$	dimensionless lithium concentration
C_{Paris}	Paris' law constant
D	lithium diffusivity
E	Young's modulus
F	crack-tip geometric function
$\mathcal{F}$	Faraday's constant
f_{w}	finite-width function
f_ϕ	crack angle function
g	stress intensity factor polynomial
G	crack-tip geometric function
h	plate half-height
i_{n}	surface current density
$\hat{I}$	dimensionless current
J	lithium concentration flux
K_{I}	stress intensity factor
K_{Ic}	fracture toughness
K_{ref}	reference stress intensity factor
l	plate thickness
m	weight function
M_1, M_2, M_3	stress intensity factor polynomials
N	fatigue cycle number
p	Paris exponent
Q	elliptic integral
r	radial position in particle
r_{max}	particle radius
$\hat{r}$	dimensionless radial position in particle
R	gas constant
S_1, S_2, S_3	crack displacement polynomials
t	time
t_{final}	time at end of charge
$\hat{t}$	dimensionless time
$\hat{t}_{\mathrm{final}}$	dimensionless time at end of charge
T	temperature
u_{r}	near-crack displacement
w	crack half-width
x	depth into plate
Y	geometric factor

Greek

α	theoretical charge capacity
θ	stress-diffusion coupling parameter
$\hat{\theta}$	dimensionless stress-diffusion coupling parameter
ν	Poisson's ratio
ρ	density
σ_{h}	hydrostatic stress
σ_{r}	radial stress
$\hat{\sigma}_{\mathrm{r}}$	dimensionless radial stress
σ_θ	tangential stress
$\hat{\sigma}_\theta$	dimensionless tangential stress
σ_0	reference load
ϕ	crack angular coordinate
Ω	partial molar volume of lithium

Appendix
Method of Weight Functions

The method of weight functions uses an integral transform to calculate stress intensity factors under arbitrary loads. First, this method requires a reference case where the crack geometry, stress profile, and corresponding stress intensity factor are all known. Then, the method of weight functions can be applied to calculate the stress intensity factor for arbitrary loading of the same crack geometry. The nonuniform diffusion-induced stress profiles due to galvanostatic cycling beg for the method of weight functions, but a satisfactory reference load for the crack geometry shown in Fig. 1 does not exist, so we use the approximate geometry shown in Fig. 2. This type of

geometric approximations typically affects the numerical value of the calculated stress intensity factor by less than 1 order of magnitude, usually on the order of $\sqrt{\pi}$.

We apply the method of weight functions to calculate the stress intensity factor, following the approach of Mattheck et al.[43] The desired stress intensity factor is calculated from the reference case as

$$K_1 = \frac{E'}{K_{ref}} \int_0^a \sigma_\theta(x) \frac{\partial u_r(x,a)}{\partial a} dx \qquad \text{[A-1]}$$

where for plane strain, $E' = E/(1 - v^2)$ and for plane stress $E' = E$. The weight function $m(x,a)$ has been defined in terms of the displacement field near the crack tip

$$m(x,a) = \frac{\partial u_r(x,a)}{\partial a} \qquad \text{[A-2]}$$

The displacement field $u_r(x,a)$ is calculated from the reference stress intensity factor by the method of Petroski and Achenbach[44]

$$u_r(x,a) = \frac{\sigma_0}{E'\sqrt{2}} \left[4F\left(\frac{a}{l}\right)\sqrt{a}\sqrt{a - x} + G\left(\frac{a}{l}\right)\frac{(a - x)^{3/2}}{\sqrt{a}} \right] \qquad \text{[A-3]}$$

where the function F is defined by the relationship

$$K_{ref} = \sigma_0 \sqrt{\pi a} F\left(\frac{a}{l}\right) \qquad \text{[A-4]}$$

and the function G is determined from self-consistency of the method

$$G\left(\frac{a}{l}\right) = \left[S_1(a) - 4F\left(\frac{a}{l}\right)\sqrt{a}S_2(a) \right] \frac{\sqrt{a}}{S_3(a)} \qquad \text{[A-5]}$$

$$S_1(a) = \pi\sqrt{2}\sigma_0 \int_0^a \left[F\left(\frac{a}{l}\right) \right]^2 a \, da \qquad \text{[A-6]}$$

$$S_2 = \frac{2}{3}\sigma_0 a^{3/2} \qquad \text{[A-7]}$$

$$S_3 = \frac{2}{5}\sigma_0 a^{5/2} \qquad \text{[A-8]}$$

σ_0 is a characteristic load of the reference case, which we have taken as uniform tensile stress. Newman and Raju[45] give analytical expressions for the stress intensity factor of the semielliptical surface cracked plate under pure tension and bending loads as polynomial functions

$$K = \sigma \sqrt{\pi \frac{a}{Q}} F\left(\frac{a}{l}, \frac{a}{w}, \frac{w}{b}, \phi\right) \qquad \text{[A-9]}$$

where Q is the elliptic integral

$$\sqrt{Q} = \int_0^{\pi/2} \left[1 - \left(1 - \frac{a^2}{w^2}\right)\sin^2 \phi \right]^{1/2} d\phi \qquad \text{[A-10]}$$

which for $a/w \leq 1$ is approximated by the polynomial expression

$$Q = 1.464\left(\frac{a}{w}\right)^{1.65} \qquad \text{[A-11]}$$

For uniform tension, which was used as the reference case for the present study

$$F = \left[M_1 + M_2\left(\frac{a}{l}\right)^2 + M_3\left(\frac{a}{l}\right)^4 \right] f_\phi g f_w \qquad \text{[A-12]}$$

$$M_1 = 1.13 - 0.09\left(\frac{a}{w}\right) \qquad \text{[A-13]}$$

$$M_2 = -0.54 + \frac{0.89}{0.2 + (a/w)} \qquad \text{[A-14]}$$

$$M_3 = 0.5 - \frac{1.0}{0.65 + (a/w)} + 14\left(1.0 - \frac{a}{w}\right)^{24} \qquad \text{[A-15]}$$

$$f_\phi = \left[\left(\frac{a}{w}\right)^2 \cos^2 \phi + \sin^2 \phi \right]^{1/4} \qquad \text{[A-16]}$$

$$g = 1 + \left[0.1 + 0.35\left(\frac{a}{l}\right)^2 \right](1 - \sin \phi)^2 \qquad \text{[A-17]}$$

$$f_w = \sqrt{\sec\left(\frac{\pi w}{2b}\sqrt{\frac{a}{l}}\right)} \qquad \text{[A-18]}$$

Under the conditions $w = a$, $b = \pi r_{max}$, and $l = r_{max}$, this reduces to

$$f_w = \sqrt{\sec\left[\frac{1}{2}\left(\frac{a}{r_{max}}\right)^{3/2}\right]} \qquad \text{[A-19]}$$

and is approximated by

$$f_w = 1 + \frac{1}{16}\left(\frac{a}{r_{max}}\right)^3 + \frac{7}{1536}\left(\frac{a}{r_{max}}\right)^6 \qquad \text{[A-20]}$$

References

1. P. Arora, R. E. White, and M. Doyle, *J. Electrochem. Soc.*, **145**, 3647 (1998).
2. Y.-I. Jang, B. Huang, H. Wang, D. R. Sadoway, G. Ceder, Y.-M. Chiang, H. Liu, and H. Tamura, *J. Electrochem. Soc.*, **146**, 862 (1999).
3. H. Wang, Y.-I. Jang, B. Huang, D. Sadoway, and Y.-M. Chiang, *J. Power Sources*, **81–82**, 594 (1999).
4. H. Gabrisch, J. Wilcox, and M. M. Doeff, *Electrochem. Solid-State Lett.*, **11**, A25 (2008).
5. Q. C. Horn and K. C. White, Paper 318 presented at The Electrochemical Society Meeting, Chicago, IL, May 6–10, 2007.
6. T. Ohzuku, H. Tomura, and K. Sawai, *J. Electrochem. Soc.*, **144**, 3496 (1997).
7. K. Sawai, H. Tomura, and T. Ohzuku, *Denki Kagaku oyobi Kogyo Butsuri Kagaku*, **66**, 301 (1998).
8. R. A. Huggins, *J. Power Sources*, **26**, 109 (1989).
9. Y. Idota, T. Kubota, A. Matsufuji, Y. Maekawa, and T. Miyasaka, *Science*, **276**, 1395 (1997).
10. I. A. Courtney and J. R. Dahn, *J. Electrochem. Soc.*, **144**, 2045 (1997).
11. F. Badway, N. Periera, F. Cosandey, and G. G. Amatucci, *J. Electrochem. Soc.*, **150**, A1209 (2003).
12. R. E. García, Y.-M. Chiang, W. C. Carter, P. Limthongkul, and C. M. Bishop, *J. Electrochem. Soc.*, **152**, A255 (2005).
13. Y.-T. Cheng and M. W. Verbrugge, *J. Appl. Phys.*, **104**, 083521 (2008).
14. Y.-T. Cheng and M. W. Verbrugge, *J. Power Sources*, **190**, 453 (2009).
15. S. Golmon, K. Maute, and M. L. Dunn, *Comput. Struct.*, **87**, 1567 (2009).
16. S. Renganathan, G. Sikha, S. Santhanagopalan, and R. E. White, *J. Electrochem. Soc.*, **157**, A155 (2010).
17. J. Christensen and J. Newman, *J. Solid State Electrochem.*, **10**, 293 (2006).
18. J. Christensen and J. Newman, *J. Electrochem. Soc.*, **153**, A1019 (2006).
19. J. Christensen, *J. Electrochem. Soc.*, **157**, A366 (2010).
20. X. Zhang, W. Shyy, and A. M. Sastry, *J. Electrochem. Soc.*, **154**, A910 (2007).
21. X. Zhang, A. M. Sastry, and W. Shyy, *J. Electrochem. Soc.*, **155**, A542 (2008).
22. Y.-T. Cheng and M. W. Verbrugge, *J. Electrochem. Soc.*, **157**, A508 (2010).
23. R. A. Huggins and W. D. Nix, *Ionics*, **6**, 57 (2000).
24. J. Wolfenstine, *J. Power Sources*, **79**, 111 (1999).
25. J. Wolfenstine, D. Foster, J. Read, W. K. Behl, and W. Luecke, *J. Power Sources*, **87**, 1 (2000).
26. K. E. Aifantis and J. P. Dempsey, *J. Power Sources*, **143**, 203 (2005).
27. K. E. Aifantis, S. A. Hackney, and J. P. Dempsey, *J. Power Sources*, **165**, 874 (2007).
28. K. E. Aifantis and S. A. Hackney, in *Nanostructured Materials in Electrochemistry*, A. Eftekhari, Editor, p. 319, Wiley-VCH, Weinheim (2008).
29. Y. Hu, X. Zhao, and Z. Suo, *J. Mater. Res.*, **25**, 1007 (2010).
30. T. K. Bhandakkar and H. Gao, *Int. J. Solids Struct.*, **47**, 1424 (2010).
31. D. P. H. Hasselman, *J. Am. Ceram. Soc.*, **52**, 600 (1969).
32. H.-A. Bahr and H.-J. Weiss, *Theor. Appl. Fract. Mech.*, **6**, 57 (1986).
33. H.-A. Bahr, G. Fischer, and H.-J. Weiss, *J. Mater. Sci.*, **21**, 2716 (1986).
34. H.-A. Bahr, H. Balke, M. Kuna, and H. Liesk, *Theor. Appl. Fract. Mech.*, **8**, 33 (1987).
35. H.-A. Bahr, H.-J. Weiss, H. G. Maschke, and F. Meissner, *Theor. Appl. Fract. Mech.*, **10**, 219 (1988).
36. S. P. Timoshenko and J. N. Goodier, *Theory of Elasticity*, p. 452–454, McGraw-Hill, New York (1970), see especially Eq. 262.
37. A. Paolone, R. Cantelli, G. Rousse, and C. Masquelier, *J. Phys.: Condens. Matter*, **15**, 457 (2003).
38. G. E. Grechnev, R. Ahuja, B. Johansson, and O. Eriksson, *Phys. Rev. B*, **65**, 174408 (2002).
39. A. Yoneda, *J. Phys. Earth*, **38**, 19 (1990).
40. D. Ravinder, *J. Appl. Phys.*, **75**, 6121 (1994).
41. D. Zhang, B. N. Popov, and R. E. White, *J. Electrochem. Soc.*, **147**, 831 (2000).
42. B. Lawn, *Fracture of Brittle Solids*, Cambridge University Press, Cambridge, UK (1998).
43. C. Mattheck, D. Munz, and H. Stamm, *Eng. Fract. Mech.*, **18**, 633 (1983).
44. H. J. Petroski and J. D. Achenbach, *Eng. Fract. Mech.*, **10**, 257 (1978).
45. J. C. Newman and I. S. Raju, *Eng. Fract. Mech.*, **15**, 185 (1981).
46. R. L. Stewart and R. C. Bradt, *J. Mater. Sci.*, **15**, 67 (1980).
47. M. Iwasa and R. C. Bradt, *Adv. Ceram.*, **10**, 767 (1984).